Liquid/liquid interface size sorted silver nanoparticles for their uniform decoration in polyindole matrix at air-water interface

6.1 Introduction

The success of π-conjugated organic polymer-based electronic devices is derived from its electronic structure, compact molecular packing and directionality of the polymer in the active layer of the device [6,7,70,95]. When fabricated via conventional film forming techniques, polymers organize themselves to have a short-range ordered microstructure in the solid film form. This self-organizing property of polymers can be explored to have a highly oriented, long range ordered polymer film [35,45,50]. The delicate balance between various intermolecular non-covalent interactions gets obstructed during solution processing of the film in many fabrication techniques. However, in LB or LS technique, where molecular ordering takes place at air-water interface, these flaws are minimized [53,54,58]. This interface based thin film processing technique has shown improvement in the conductivity of various polymers due to enhanced degree of ordering (molecular packing), which in turn leads to improved device performance [69]. It will not be out of place to mention that it is important to regulate the ordering of polymers at all levels of hierarchy starting from synthesis. At all levels, the presence of structure functionality and π-conjugation in the building blocks (monomer unit) drive the specific thermodynamic force of interactions, which assist the polymer assembly [35].

Further, it has been reported that some conducting nanomaterials or NPs when incorporated into CP matrix, their assembly and molecular packing (π-π stacking) have drastically improved, thus leading to augmented charge transport properties via charge

transfer interaction [8]. In recent years NP synthesis has seen advances leading to higher purity, larger yield, better size dispersion and shape, controlled functionalization, monocrystallinity, etc. just to name a few [13,14,20]. NPs can be synthesized through all the known routes of materials synthesis viz. chemical, physical and physiochemical just by providing optimal conditions for arresting growth of the forming nuclei [13-15,19]. Colloidal synthesis though, by far is the cheapest and most facile method of NP synthesis for quick application in experiments. Metal NPs are further exciting owing to their already demonstrated usage in electronics, medical imaging and diagnosis, sensory applications, customizable optical properties [15,99]. As compared to other metals, Au and Ag, have been explored much due to their easy reducibility, safe electrochemical window to work with; stupendous electro-catalytic behaviour; amazing affinity towards Sulfur and Nitrogen; high conductivity and most prominently their operational stability. Moving down to lower dimension i. e. from bulk to nano level, the properties of noble metals greatly enhance due to extremely large surface area. AuNPs have been explored much for various applications, but its high cost repudiates its merits. Liquid-processed AgNPs hence represent an appealing cost-effective approach. There are many systems that involve materials whose activities are greatly enhanced when incorporated with AgNPs but have a limitation of being soluble only in water. Synthesizing and stabilizing NPs in a liquid colloidal state requires them to be protected from physical aggregation and chemical degradation by providing either steric or electrostatic cushioning. This has been reportedly achieved through surface passivation or coating the NPs with an inert material monolayer [13-15]. Large number of organic solvents can provide a non-hostile chemical environment for stabilizing NPs using an appropriate soluble agent to protect the NP from aggregating [148]. Organic solvents hence have also been shown to exhibit a large number of synthesis protocols in the existing literature. Some very reputed quick

synthesis of NPs have been reported being facilitated by phase transfer from either aqueous to organic or vice-versa by depositing hydrophilic or hydrophobic monolayer over it [19,22,23]. In our current study, we are demonstrating that interface of two immiscible solvents (water - chloroform) can be effectively used as a size-sorter in selectively obtaining the required particle size of the synthesized product facilitated through an appropriate PTA. In our experiments, an increasing median particle diameter has been obtained with increasing concentration of the PTA. The structure of PTA should be such that it must possess an open-faced binding space to allow (van der Waals) interaction between the counter-ion and the cation (N+). The opposite end must offer steric screening effect to prevent close approach of the counter ion in order to obtain binding specificity. Quaternary ammonium salts such as CTAB, TOAB, DDAB, etc are efficient PTAs associated with advantage of being soluble in polar organic solvents unlike other capping agents that are restricted to non-polar solvents. But the peculiar geometry of DDAB possessing two methyl groups and two large alkyl chains fascinated the most for its selection [22]. Smaller alkyl groups aid in occupying the position near interface thus creating higher concentration there. This reduces surface pressure and aids in phase transfer. DDAB being a highly lipophilic PTA prefers to be entirely in the organic phase attributed to hydrophobic pressure experience by long alkyl chains [149]. Our selection of biphasic two-pot synthesis circumvents a post synthesis difficulty of removal of counter/extra ions and other unknown water-soluble entities. The expedient function of DDAB molecule negates the need of an external agent needed for stabilizing the organic colloid and saves another post-processing step. AgNPs synthesized in aqueous phase utilizing sodium borohydride is cost effective and well established method already been reported in literature; but associated with demerits of polydispersity and lower stability. So, the first objective of this work is to establish a cheap and facile

approach for obtaining silver NPs in organic phase as well as obtain size selectivity utilizing DDAB as both PTA and stabilizer.

Further the advantageous property of AgNPs has been explored for nanohybrid formation with CPs. The nanohybrid formation can be achieved via phase transfer of AgNPs from aqueous to organic medium (chloroform), which facilitate the CP processing. For AgNPs blended with polymers it is observed that their self-assembly dynamics decelerates due to the formation of traps (or spaces) developed in the assembled structures. These traps, arising due to polymer interactions, can be annealed out successfully via thermal techniques, however this makes this process not suitable for organic polymers or polymer based flexible electronic devices [19,21]. Therefore, a controlled nanostructure assembly technique is highly desirable. Moreover, Langmuir-Blodgett/Schaefer method is amongst the better methods which involves compression of the floating monolayer uniaxially leading to nanostructures assembly and packing over the water subphase, overcoming the drawbacks of other popular polymer processing techniques.

Among the various π-conjugated polymers, PIn and its derivatives possess excellent electroactivity, environment stability, excellent thermal stability, easy degradation, etc. Several research groups have demonstrated the enhancement in PIn conductivity upto several orders of magnitude by composite formation [18,55,63,69,76]. Despite this, there is a lack of report on AgNPs as well other metal NPs incorporation and composite formation with polymer via Langmuir technique. Incorporation of metal nanostructure in polymer matrix enhances the photophysical and charge transport property of polymers, which is highly desirable for large area and optoelectronic devices like solar cell, photovoltaic cells etc. [99]. This motivated us to be the premier in utilizing Langmuir

method for uniform distribution and assembly of AgNPs in PIn matrix at air-water interface forming nanohybrid and annealing out the traps by very slow compression of the film. This approach has proved to be expedient in three ways. First, possession of self-organization property of the AgNPs may act as a template for preorganization of polymers, facilitating their ordering via Langmuir. Second, AgNPs contribute in charge transport property enhancement of the nanohybrid LS films formed. Third, successive slow compression of the Langmuir layer enables sufficient time for relaxation and filing up the spaces (traps) of the nanohybrid and thus resulting in its increased ordering and crystallinity [53,54,58].

This work demonstrates the exploitation of both self-assembling properties of AgNPs and the langmuir interface for orienting PIn film structure. Langmuir stable films produced are investigated for their AgNPs distribution in polymer matrix via TEM and AFM. Both these features contribute to the enhancement in the molecular packing (π-π stacking), ordering, photophysical and charge transport property of the Ag-PIn nanohybrid LS films verified via SERS, XPS and current-voltage relationship.

6.2 Results and discussion

6.2.1 Spectroscopic analysis of silver nanoparticles

A distinct biphasic system obtained immediately after adding aqueous synthesized AgNPs to chloroform with varying DDAB concentration is shown in Figure 2.5. The synthesis of AgNPs is observed under UV-Vis spectroscopy. A typical representative absorption spectra of pure silver hydrosol, supernatant aqueous phase and chloroform sub-phase (after phase transfer) along with solvents are shown in Figure 6.1. Typical SPR peaks (408 nm) are observed with a red-shift for AgNPs in supernatant aqueous phase

and chloroform sub-phase (obtained after vigorous shaking and allowing phase transfer using 5 mM concentration of DDAB) in comparison to pure silver hydrosol (388 nm). A similar pattern was observed for all other concentrations of DDAB (10, 25, 50 and 75 mM) used in the experiment. The red shift in AgNP SPR peak with respect to original hydrosol is accounted for change in environment of the NPs with electron deficient moiety-quaternary ammonium cation-capping the AgNPs, owing to decrease in Fermi level on withdrawal of surface electron density [19,21,23,30].

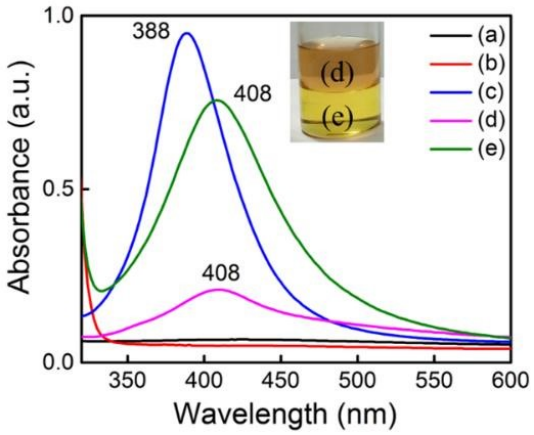

Figure 6.1 UV-vis spectra of (a) deionised water, (b) chloroform, (c) pure silver hydrosol, (d) supernatant aqueous phase (after phase transfer; shown in inset) and (e) chloroform subphase (after phase transfer; shown in inset).

To further understand the nature of molecular interaction and predict the physiochemical reaction mechanism, the FT-IR and XPS was used. Vibrational spectra gave an insight on stabilization of silver NPs with DDAB as stabilizing agent in organic phase comparing it with pure DDAB. Characteristic vibration peaks of DDAB at 721, 886, 1467, 2852, 2919 cm^{-1} for methylene along with that of methyl at 2,954 cm^{-1} were evidently observed in Figure 6.2 (a) [150]. The methylene (asymmetric and symmetric stretching) vibrations (Figure 6.2 (b)) for DDAB-protected silver NPs are little shifted to 2855 and 2923 cm^{-1}

signifying the sufficient surface coating of DDAB on the silver NPs [151]. Moving towards lower-frequency region, the peaks located at 1467 and 721 cm^{-1} assigned to the scissoring motion (H-C-H bending) and rocking mode of the methylene chains for pure DDAB, are also observed for DDAB protected silver NPs with small shifts. Peak observed around 1205 cm^{-1} corresponds to C-N stretching in both the spectra. Peak at 886 cm^{-1} for pure DDAB corresponding to in-plane CH_3 rocking mode is also present for DDAB-protected silver NPs at 891 cm^{-1}. Retention of these vibrations with minor shifts in organosol ensures the association of stabilizer molecules with the silver NPs [151,152].

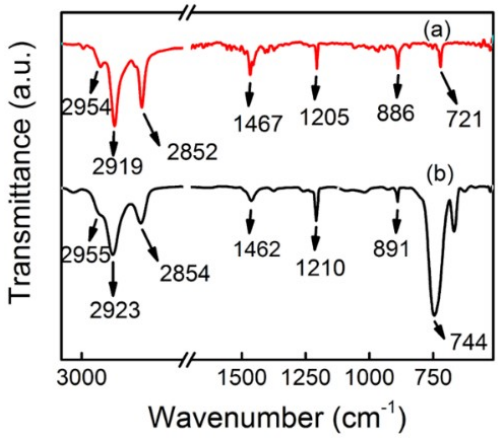

Figure 6.2 FT-IR spectra of (a) pure DDAB (b) silver organosol.

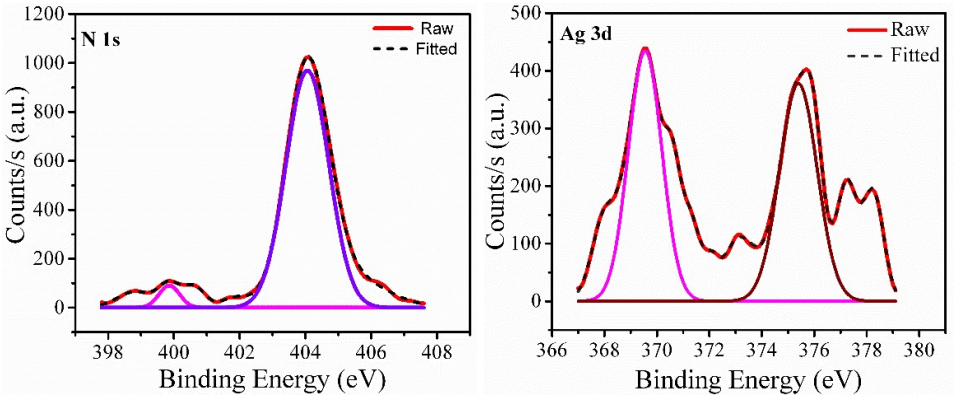

Figure 6.3 XPS spectra of silver organosol.

The XPS spectroscopy (as shown in Figure 6.3) reveal the silver to exist in its metallic state with $Ag3d_{5/2}$ and $Ag3d_{3/2}$ orbital electrons bound at 369.5 eV and 375.7 eV respectively which resembles well with the existing literature [153]. Peaks at binding energy of 400 eV and 404.1 eV further strengthen our predicted mechanism of quaternary ammonium cation capping AgNP surface as the spectrum closely resembles to existing XPS information [154]. The characterization of silver hydrosol, final organosol and supernatant aqueous phase post phase-transfer of silver NPs confirms the proposed hypotheses (i) occurrence of phase transfer of silver NPs and (ii) a certain degree of size-selectivity in the phase transfer process.

6.2.2 Structural investigation of AgNPs

X-ray diffraction (XRD) on a solid film prepared off the organosol by drop-casting it on a glass cover slip and allowing the chloroform to evaporate reveal the low intensity peaks corresponding to polycrystalline silver particles (as shown in inset of Figure 6.4) and high intensity peaks for crystallites of DDAB owing to very high relative concentration. The

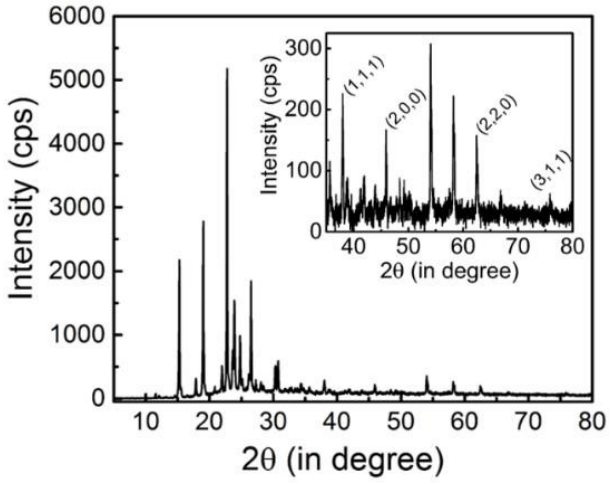

Figure 6.4 XRD pattern of silver NPs in organic phase. Inset shows amplified diffraction pattern corresponding to (111), (200), (220) and (311) planes of fcc silver.

XRD pattern of organosol recorded was characteristic of pure silver (as shown in Figure 6.4). The observed peaks correspond to the diffraction pattern of face centred cubic silver, (JCPDS; file no. 04-0783) and can be indexed to (111), (200), (220) and (311) planes. Some high intensity peaks in the wide XRD spectrum seen can be identified as of DDAB crystallites (with peaks at 2θ value close to 148, 188, 238, 258) [150].

TEM images were recorded for silver hydrosol as well as for silver colloid in organic phase. Hydrosol image (as shown in Figure 6.5 (a)) represented agglomerated nanoclusters with varying size of 5 to 50 nm. Wheras TEM micrographs (Figure 6.5 (b)) for organosol show long-range order and self-assembly of NPs up to 0.5 μm in dimension in organic medium as opposed to random distribution and agglomeration obtained for aqueous phase. A near constant inter-particle distance close to 2.4 nm exists in the assembly pointing towards the NPs being protected by a moiety. A bilayer thickness of DDAB has been reported to be 2.4 nm, which is approximately twice the length of alkyl chain of DDAB thus confirming a monolayer coating of DDAB on AgNPs in our experiments [155]. This is a clear indication of self-assembly facilitated by balance between attractive inter-particle force and steric hindrance from DDAB coated alkyl chains. In solution (organic) phase, DDAB stabilized NPs are randomly dispersed, the weak attractions between NPs are expertly partitioned, but as soon as the solvent evaporates these relatively weak forces come into action thus initiating the assembly of NPs. Overall, after solvent drying the NPs form a 2D array of self assembled nanostructures [156]. The same carbon-coated copper grids holding samples for TEM were used to obtain SAED image of the materials. Insets of Figure 6.5 (a) and (b) show the diffraction pattern of polycrystalline Ag from hydrosol and organosol respectively [157]. The diffraction pattern in hydrosol is more distinct as the AgNPs are bare and in

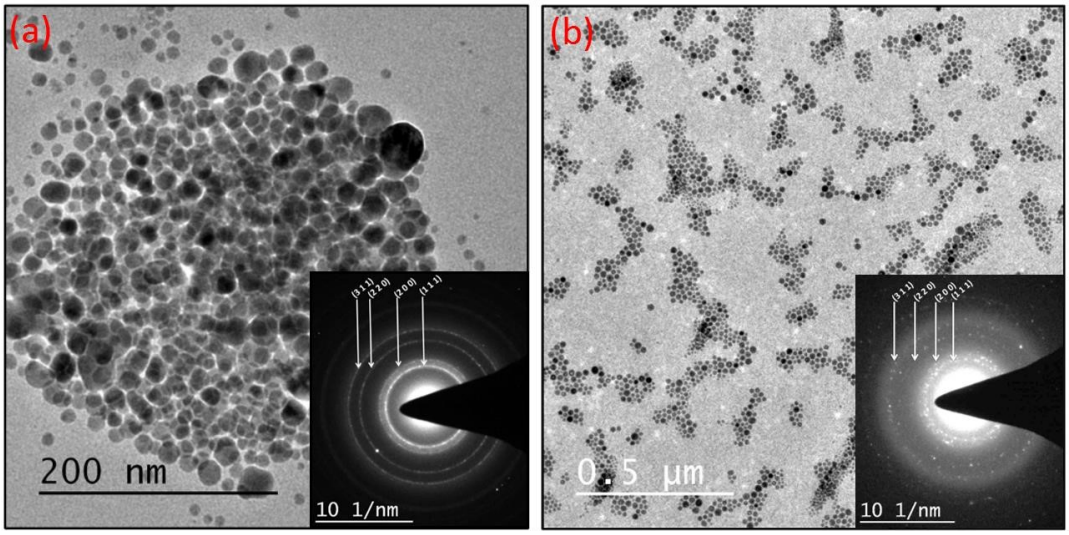

Figure 6.5 TEM image of (a) silver hydrosol (inset: SAED pattern) (b) silver organosol (inset: SAED pattern)

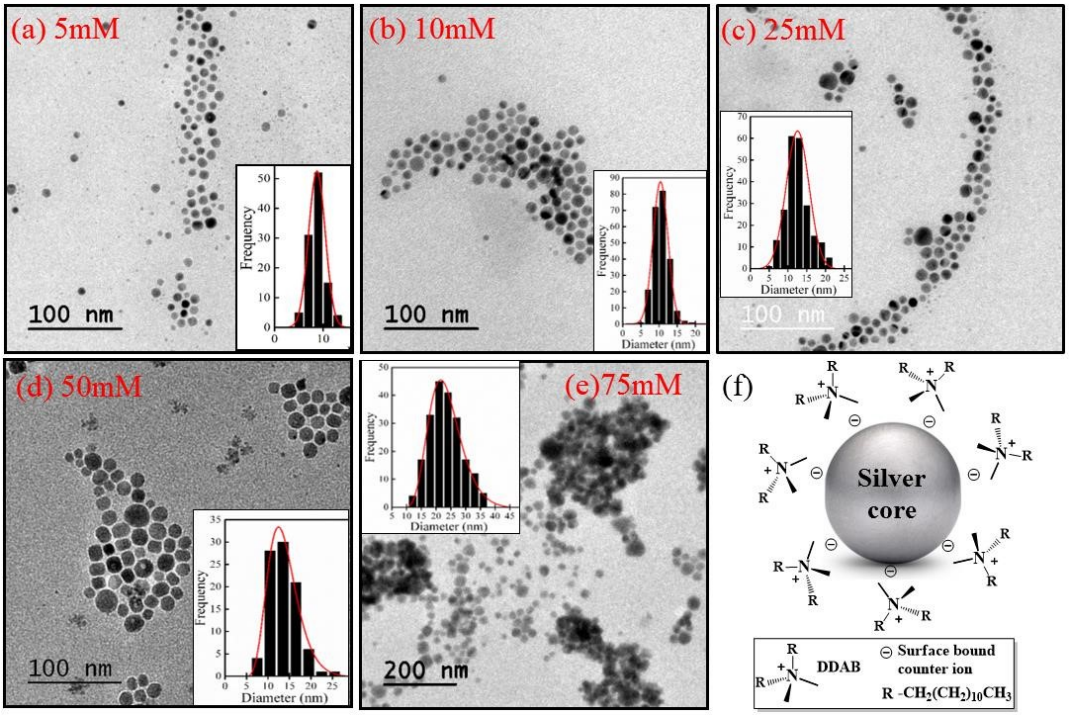

Figure 6.6 TEM images of silver colloid in organic phase (inset: histogram depicting PSD) with varying DDAB concentration namely (a) 5 mM (b) 10 mM (c) 25 mM (d) 50 mM (e) 75 mM and (f) plausible structure for DDAB acting as AgNP stabilizer.

large numbers while the silver suspension in chloroform is selectively transitioned through interface, so less in quantity and covered by high surface concentration of DDA ions. The diffraction patterns in both the cases show the crystal structure for silver and high intensity peaks have been accordingly indexed. XRD pattern also elucidated the presence of DDAB and AgNPs in organic phase as shown in Figure 6.4. The diffraction ring from the AgNPs are present in a more prominent way because of the silver being an electron rich metal in comparison to DDAB which contributes as a hazy background.

Figure 6.6 (a-e) shows TEM micrograph for each DDAB concentration (5, 10, 25, 50 and 75 mM) and the size of AgNPs was estimated via Image Analysis software from counting of 200 particles for each. The results obtained were used to generate histograms which was fitted with most appropriate model (Gaussian/Log-normal) to obtain median particle dimension values that shown in insets of Figure 6.6 (a-e). Median particle size (particle size distribution, PSD) as obtained from the curve fitting has been taken as average particle size of the phase transfered NPs. Mean particle size has also been calculated, which turns out to be within the range of 0.1 nm making them nearly equal to median particle size. For sake of simplicity, only median particle size has been mentioned here. The trend is seen as follows for median particle dimension 8.7±2.0; 10.4±2.4; 12.6±3.5/12.3±3.2 (Gaussian fitting/LogNormal fitting); 13.3±3.6 and 22.8±5.8 nm over varying concentration of DDAB as 5, 10, 25, 50 and 75 mM respectively. It is interesting to observe that with increasing concentration of DDAB used as PTA, not just the median particle dimensions obtained shifts to higher values but the peak width also increases, depicting lenient selectivity towards a particle dimension at higher concentration. The distribution of particle frequency over dimensions for lower concentrations (5, 10, 25 mM) of DDAB follows Gaussian distribution better. While at higher concentration (50,

75 mM) the distribution is Log-Normal which is a general distribution of NPs produced through reduction corresponding salts [158]. This slight deviation of theoretical particle distribution model also approves a size sorting behaviour across solvent interface as demonstrated. Figure 6.6 (e) shows how the AgNPs get agglomerated at use of large concentration of PTA (surfactant) which is observed in the sample transitioned using 75 mM DDAB solution. We could observe a shift in median particle dimension to larger size with increasing DDAB concentration. This can possibly be accounted to combined effect of varying surface to volume ratio of particles. A higher surface area-volume ratio for smaller NP size results in larger hydrophobic force acting on the NP and thus forcing a phase transfer [159].

On contrary larger particles due to smaller surface area-volume ratio experiences a weaker hydrophobic push. The free energy of solvation is another factor accounting for smaller NPs being selectively transitioning and stabilizing in the preferred solvent. Through Monte Carlo (MC) and DFT it is predicted that solvation free energy increases with size of the particle i.e. it becomes energetically expensive to accommodate larger NP in a solvent [160].

The TEM micrographs and corresponding PSD confirms the varying median particle size as well as width of the distribution curve indicating a size-selectivity phenomenon. The linear trend of increasing median particle size as a function of increasing DDAB concentration reinforces the observation of aqueous-organic immiscible interface acting like a size-sorter. This size sorting is assisted by the hydrophobic hydrophilic force gradient experienced by particles undergoing phase transfer.

A trend curve as represented in Figure 6.7 was plotted to summarize the results obtained in Figure 6.6. The curve depicts the Gaussian fit size-range to be smaller for lower DDAB

concentrations. While moving towards higher concentration, the size-range obtained via Log-normal fit is desirable as explained earlier. Hydrosol contains particles with size-range of 5-50 nm. The particle size distribution is indeed log normal when all the formed particles will be considered. But after phase transfer, a small fraction of these particles are transferred to the organic phase and hence the normal (Gaussian) fit better till this transferred bandwidth is small. As the transferred size bandwidth increases the initial log-normal distribution fits better for higher concentration of DDAB. A particular size window of AgNPs are transitioned with different DDAB concentration. Thus, this trend can be useful in picking up the required DDAB concentration to obtain silver nanoparticles dimension as per the choice of the application. This can be very useful in predicting the dimensions of particles to be synthesized out of wet colloidal synthesis which could dramatically lower the time and cost required for preparation of metal NPs such as Ag, Au,etc.

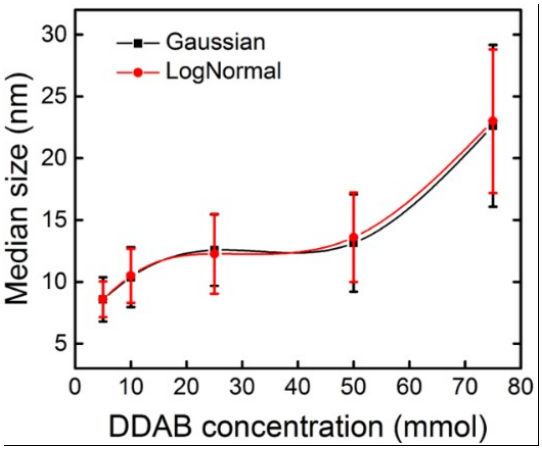

Figure 6.7 Trend of increasing median particle dimension (diameter) and the corresponding width of distribution represented as error bars.

6.2.3 Characterization of silver-polyindole (Ag-PIn) nanohybrid

Ag-NPs formed in aqueous phase (hydrosol) and phase transferred to chloroform

(organosol) were characterized for their size, morphology and particle size distribution as described in section 6.21 and 6.2.2. Further, silver organosol when added to PIn displays its persistent SPR signature (silver) merging with the n-π* transition of PIn (Figure 6.8 (a)). As compared to pure PIn spectra, there is a red shift in its characteristic π-π*, n-π* and polaronic transitions for the nanohybrid [18,63,69,76,79]. These results point towards increased conjugation length in the nanohybrid. Figure 6.8 (b) displays FT-IR spectra for pure PIn and Ag-PIn nanohybrid. Characteristic vibrations of PIn are also observed for Ag-PIn enlisted in Table 6.1 with some significant shifts towards higher wavenumber [63,75,76]. Both findings show red shift indicating an increase in conjugation length, which means there is a significant influence of Ag in the molecular packing.

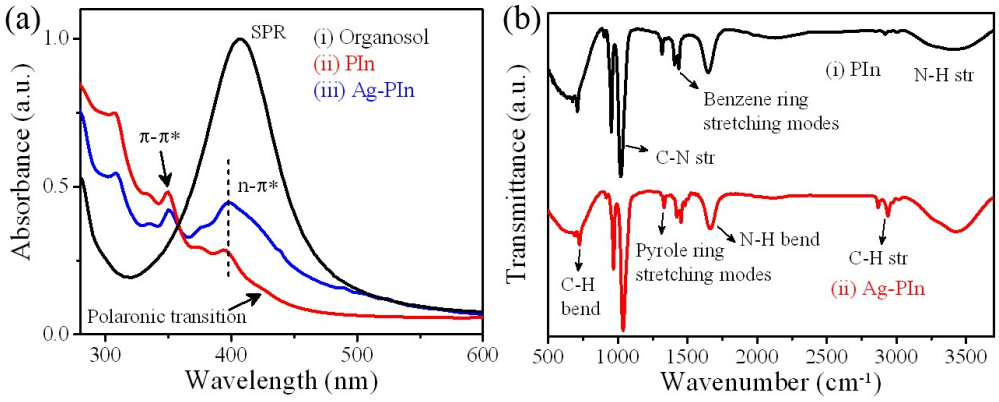

Figure 6.8 (a) UV-Vis spectra of (i) organosol (ii) PIn, (iii) Ag-PIn, and (b) FT-IR spectra of (i) PIn and (ii) Ag-PIn.

Table 6.1 Vibrational band assignment of PIn and Ag-PIn.

S.No.	Band assignment	Vibration frequency (cm^{-1})	
		PIn	Ag-PIn
1	N-H stretching and deformation	3382, 1646	3428, 1661
2	Stretching modes of the benzene ring	1437	1452
3	Stretching mode of the pyrrole ring	1317	1331
4	C-N stretching	1020	1037
5	C-H deformation benzene ring (oop)	709	723

6.2.4 Langmuir floating film studies

Figure 6.9 (a) displays SP vs area/molecule (π-A) isotherm for PIn and Ag-PIn nanohybrid. After the sample solutions of both (pristine PIn and Ag-PIn nanohybrid) are spread on the air-water interface, the barriers are automated for compressing along interface at the rate of 10 mm/min. As the monolayer (actually pseudomonolayer) is compressed, its area decreases and corresponds to phase transition indicated by slope changes in the isotherm. At low surface pressures, the monolayer consisting of far apart molecules behaving like gaseous phase and with a gradual increase in surface pressure, a clear transition from liquid to liquid condensed and then to the solid phase is observed. Accordingly, isotherms observed for both have been divided into various regions and a schematic is representing each phase of isotherm is shown beside it [67,99,161]. Region I resembling gaseous phase (molecules far from each other; negligible interaction); II denoting liquid (molecules approach each other and assemble themselves); III representing liquid condensed phase (molecules just close enough forming compact arrangement); and IV resembles collapse region in which monolayers start overlapping due to excess pressure. Overall region III (plateau) represents the most appropriate one for films to be lifted on solid substrates. Analysing the isotherms, it is seen that the start point of both PIn and Ag-PIn entering the liquid phase are different (16.5 and 26 $Å^2$ respectively). This indicates that silver incorporated in PIn matrix occupies larger surface area than PIn alone. This again signifies that there is greater π-π stacking in Ag-PIn chain after solvent evaporation.

Langmuir films deposited from single compression step on solid substrates immobilize the monolayer structures that may not be sometimes stable at the air-water interface. The stability of these films can be investigated when the film is monitored under constant area

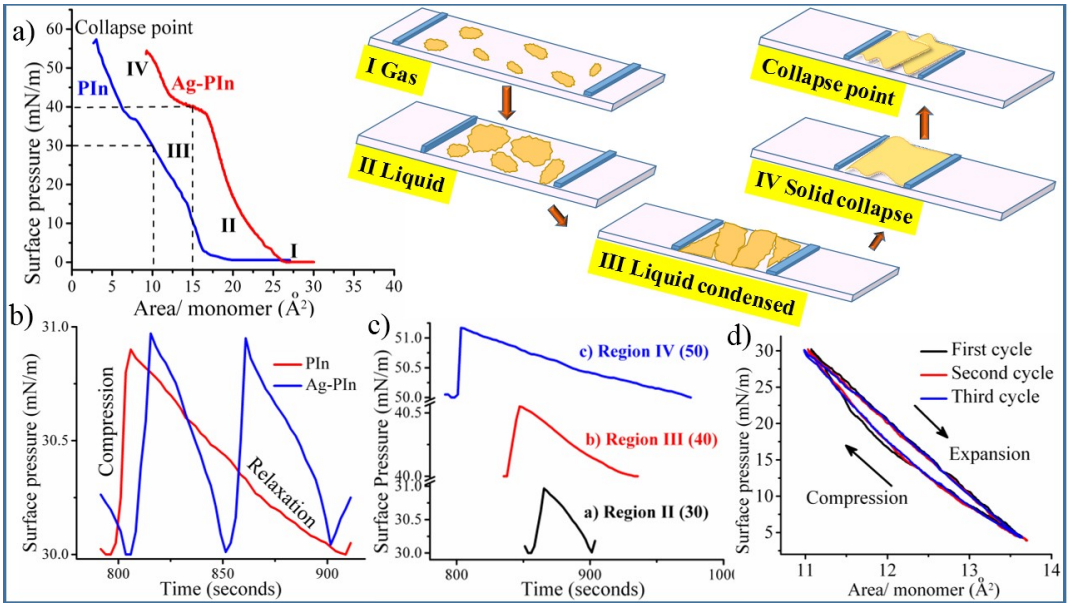

Figure 6.9 Pressure vs area (π-A) isotherm for (a) PIn, and Ag-PIn along with schematic depicting the phenomena at various regions, (b) compression-expansion curve for PIn and Ag-PIn nanohybrid at SP=30 mN/m, (c) compression-relaxation phenomena at three different SPs (30, 40, and 50 mN/m) from different regions (II, III and IV) of the isotherm, (d) compression-relaxation cycle of Ag-PIn film.

over time. Stability of the films formed is the deciding parameter for uniform film formation before its deposition, which is done by monitoring the surface pressure compression-relaxation process [29,53,54,58]. We have shown in Figure 6.9 (b), the compression-expansion curve for PIn and Ag-PIn nanohybrid at a particular SP (30 mN/m). Three observations made from this graph were: (1) area under the curve is smaller for Ag-PIn in comparison to PIn, (2) compression curve slope is similar for both, and (3) relaxation curve is steeper for Ag-PIn. This clearly denotes that nanohybrid takes lesser time to come back to its original state, so it is more compressible as compared to PIn and can be accounted to stronger intermolecular (non-covalent) interactions between silver and PIn. For better insight into the film stability of the Ag-PIn nanohybrid, we

investigated compression-relaxation phenomena (Figure 6.9 (c)) at three different pressures (30, 40, and 50 mN/m) from different regions (II, III and IV) of the isotherm. After spreading the sample solution, the barriers were automated to compress the monolayer up to 30, 40 and 50 mN/m SP and the variation of surface pressure in same time duration has been plotted for each respectively. At low surface pressure i.e. 30 mN/m (region I) the relaxation curve drops down sharply. This denotes that molecules being far apart do not show cooperative motion. At 40 mN/m (region II), relaxation curve decays in a longer time and finally, for 50 mN/m (region III), larger surface pressure range, longer relaxation time and larger area under the curve as compared to region II were observed. This behaviour can be explained by considering the intermolecular interactions. The film held at SP 40 mN/m behaves like an elastic stretched membrane and it retracts its original form faster (100 s) as compared to 50 mN/m SP (175 s). SP in region III is just sufficient for the molecules to be held together by intermolecular (non-covalent) forces. These observations motivated us to opt SP 40 mN/m as the optimum one for film deposition.

Further, this has been elaborated by monitoring the compression-relaxation cycle (Figure 6.9 (d)) to validate the Ag-PIn nanohybrid film compressibility. For this measurement, SP 30 mN/m (just below the deposition pressure) was chosen. We observed that all three cycles track nearly the same path with minor differences from each other. This traceability signifies that intermolecular (non-covalent) forces play a dominant role such that successive compression and expansion of the Langmuir monolayer does not distort the film stability significantly [53,54,58].

6.2.5 Structural study of Langmuir films

Figure 6.10 (a) shows the TEM micrograph of a single time lifted layer (1L) LS film of

PIn lifted at 30 mN/m SP on carbon-coated TEM grid with SAED in the inset. It reveals a large continuous sheet structure film formed at the air-water interface. Figure 6.10 (b) shows its magnified image. There is some pattern forming fringes which locate to d-spacing of 0.344 nm (calculated via Gatan Digital Micrograph software in inset). This value relates to the π- π stacking distance between the two PIn chain backbones [35,162]. Also, SAED pattern forming ring-like structure reveals the formation of ordered microstructures in the film [35].

Initially, when these two components (AgNP and PIn) were mixed to form a nanohybrid, the distribution was random like that shown in TEM image (inset: SAED pattern), HAADF image and elemental mapping (Figure 6.11) of drop cast Ag-PIn nanohybrid film. Ag-PIn nanohybrid LS films were also lifted similarly at 40 mN/m SP on a TEM grid and investigated for its distribution pattern of silver in the PIn matrix. Figure 6.12 (a) informs us about the large area uniform distribution of silver particles in PIn with its SAED (inset) validating the film crystallinity. Surface area coverage of AgNPs in the PIn matrix from TEM micrograph was calculated and found to be 34.6±3 %. Its magnified image in Figure 6.12 (b) shows that region 1 and region 2 (marked in square) correspond to the AgNP and PIn respectively in real space. Their d-spacing was calculated via GATAN software and found to be 0.228 nm characteristic of silver and d=0.328 nm for polymer region. For both square regions 1 and 2, Fourier transform being simultaneously captured clearly justifies them. As compared to Figure 6.10 (b), for polymer region, d-spacing tends to decrease in this case. This reveals the decrease in π-π stacking distance between neighbouring backbones. This decrease can be accounted to the silver playing a significant role in the ordering of polymeric chains, thus leading to better molecular packing [162]. On comparing the micrographs in Figure 6.11 and 6.12, we can analyse

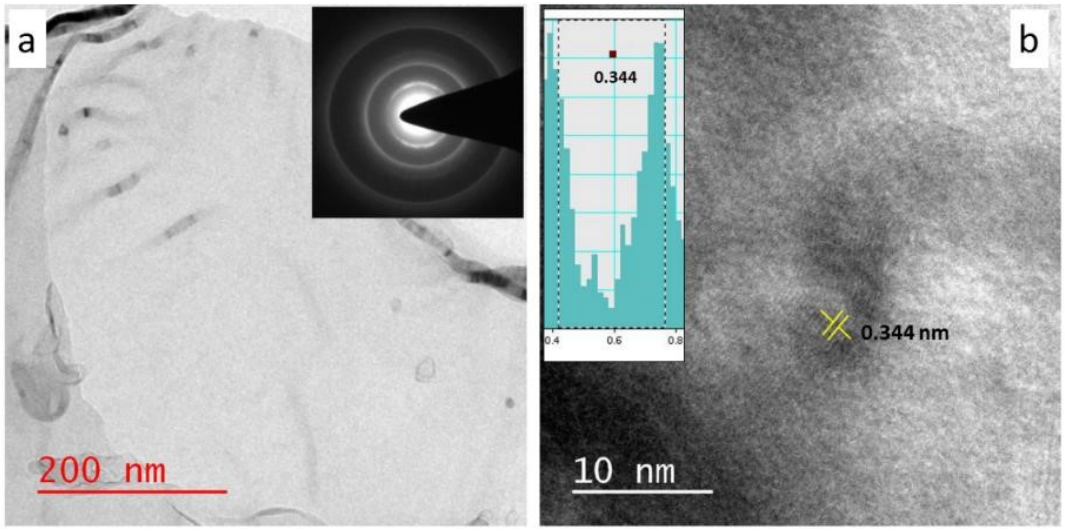

Figure 6.10 TEM micrograph of a single time lifted layer PIn LS film at 30 mN/m SP at (a) low magnification (inset: SAED) and (b) high magnification (inset: d-spacing).

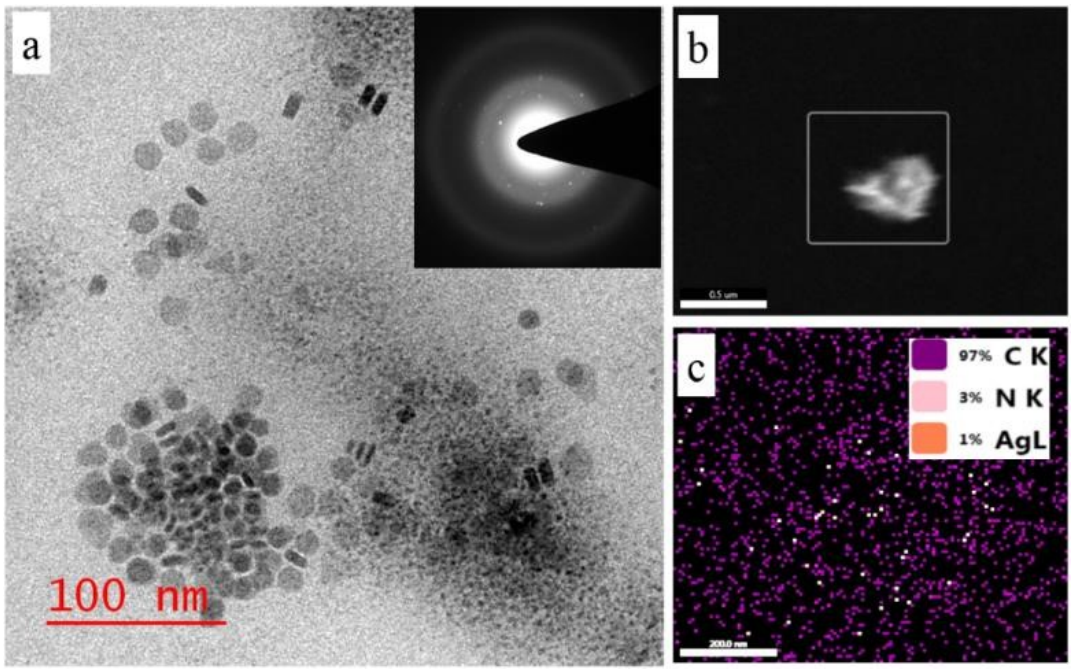

Figure 6.11 (a) TEM image (inset: SAED pattern), (b) HAADF image and (c) elemental mapping of drop cast Ag-PIn nanohybrid film.

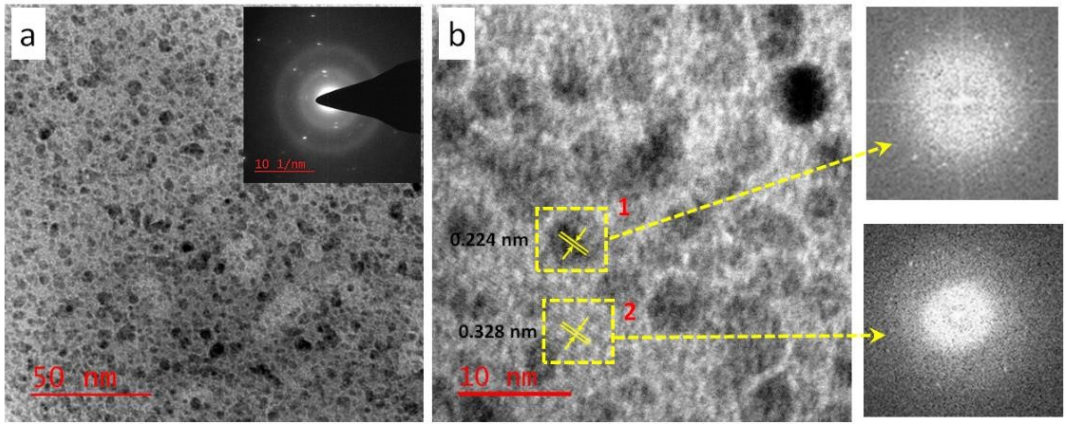

Figure 6.12 TEM micrograph of AgNP-PIn Langmuir film deposited at 40 mN/m at different magnification scale (a) 50 nm and (c) 20 nm; FT of Region 1 and 2.

the role of Langmuir technique in nanocomposite formation of the silver and PIn at the air-water interface. When the nanohybrid was drop casted on water and allowed to assemble at air-water interface via Langmuir technique, various operating factors cooperated in its assembly. First, the spread of very dilute solution on interface prevented its molecular aggregation; second; very slow barrier compression speed (10 mm/min) enabled its forced assembly thus bringing molecules closer; third, intermolecular forces (non-covalent) operational as the monolayer was being compressed; fourth, excellent self-assembling property of silver embedded in the polymer matrix. After these forces being operative in Langmuir trough, the wilhemy plate sensed various phases of the monolayer on compression. The LS films being lifted at optimum SP (already discussed above) displayed the uniform distribution of these nanoparticles in PIn matrix, thus leading to the formation of a nanocomposite at the air-water interface.

To determine the structure and orientation in the film, we have utilized GI-WAXS measurement for both PIn and Ag-PIn LS films shown in Figure 6.13 (a and b) respectively. The 2D q-plots clearly show a GI-WAXS pattern which indicates lamella,

oriented parallel to the sample's surface, for both samples. For Ag-PIn sample, in contrast, shows oriented Bragg peaks in the WAXS-regime which indicates a higher degree of orientation with π-π stacking orientation parallel to the surface of the substrate as revealed in TEM above (Figure 6.12). So, Ag-PIn films formed are more crystalline than PIn LS films, and the enhanced orientation in the film also results in extension of π-electron overlapping which is required for mobility enhancement in semiconducting organic molecule-based electronic devices [163,164].

6.2.6 Surface characterization of LS films

Surface analysis of PIn and Ag-PIn LS films has been investigated through AFM

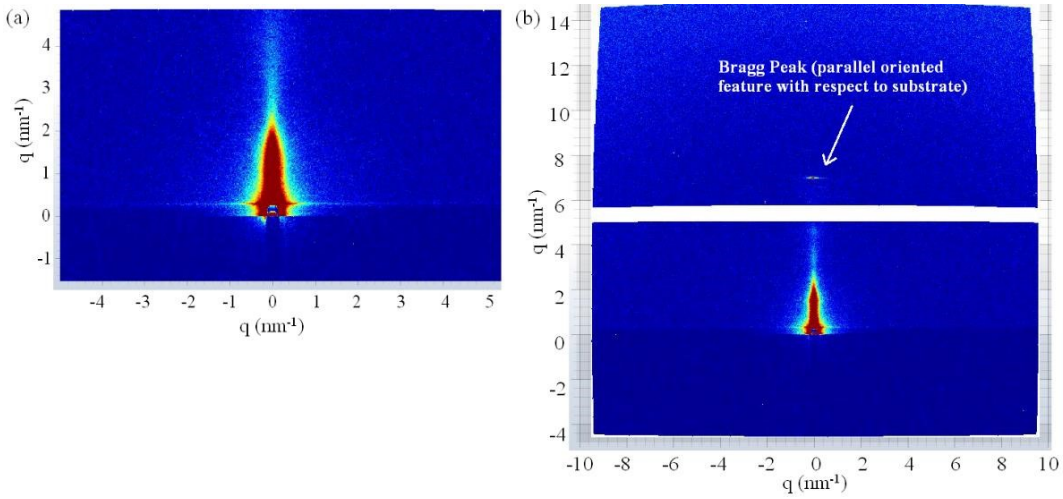

Figure 6.13 GIWAXS 2D q plot of (a) PIn and (b) Ag-PIn LS film.

in tapping mode. The 3D AFM topography and phase images scanned simultaneously in the same region, are shown in Figure 6.14 (a and c) and 6.15 (a and c) respectively. To get a proper understanding of the surface roughness, root mean square (RMS) value of the surface roughness was computed using Nanotech software. The surface roughness of both the films follows the Gaussian distribution [165].

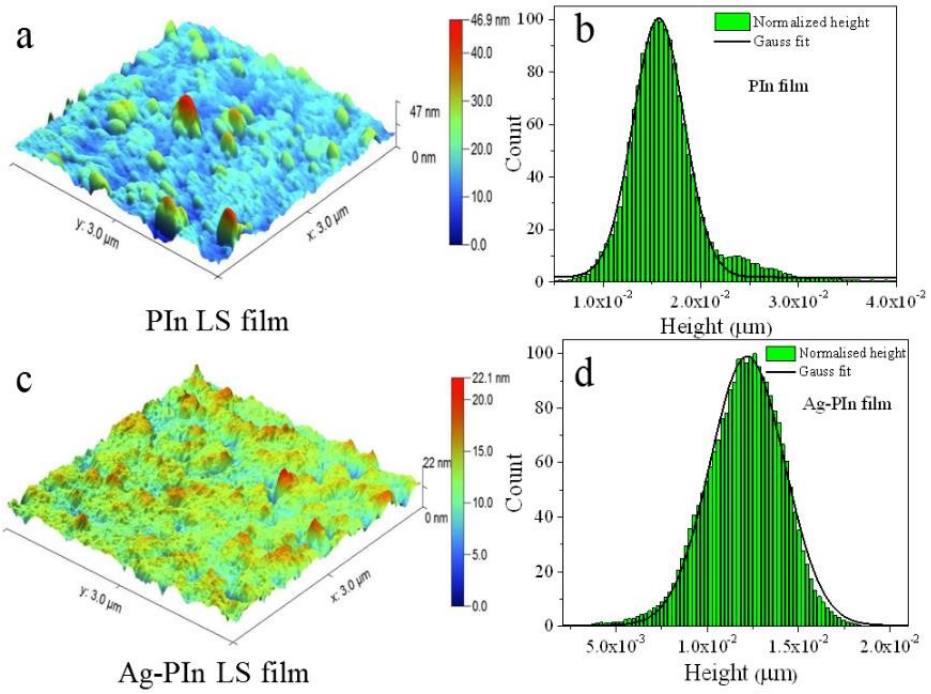

Figure 6.14 Tapping mode atomic force micrographs of (a) PIn and (c) Ag-PIn Langmuir film deposited at 30 and 40 mN/m respectively with their corresponding (b) and (d) roughness distribution.

Table 6.2 Surface analysis parameters obtained from AFM and KPFM.

Film Composition	**R.M.S. Roughness, $R_{r.m.s.}$ in nm**	**Mean roughness, R_a in nm**	**Standard deviation, σ**	**Dc in nm**	**Average Contact Potential Difference, V_{CPD} in Mv**
PIn	4.354	2.974	5.24	15.68	2.560
Ag-PIn	1.868	1.428	4.07	12.19	1.373

The roughness distribution for the PIn and Ag-PIn Langmuir films is shown in Figure 6.14 (b and d), and all the findings are being tabulated in Table 6.2. A decrease in surface roughness as well as average grain size for Ag-PIn Langmuir film as compared to pristine PIn film (Figure 6.15 (b and d)), suggests that the Ag incorporation reduces the PIn molecule aggregation probability. In case of pristine PIn film, molecules aggregate

forming pseudomonolayer. Whereas in Ag-PIn layer, Ag facilitates the smooth uncoiling (expansion) of PIn chain. This justifies the need of higher surface pressure per unit area for monolayer formation in case of Ag-PIn Langmuir film [18,63,76].

For investigation of film surface property on the macroscopic scale and to determine its behaviour on water subphase, we have measured its contact angle with respect to water. For this study, we have lifted LS films in two ways. First, stamping from above the water surface that has been named as Type 1 film, second from below the water surface (Type 2). A schematic (Figure 6.16 (a)) has been shown for a better understanding. As per previous works, the polar part (hydrophilic) of the molecule tends to interact with water subphase directing the hydrophobic part away from the surface [53,54,58]. As in the case of PIn, the electron density is concentrated around the nitrogen of pyrrole ring thus

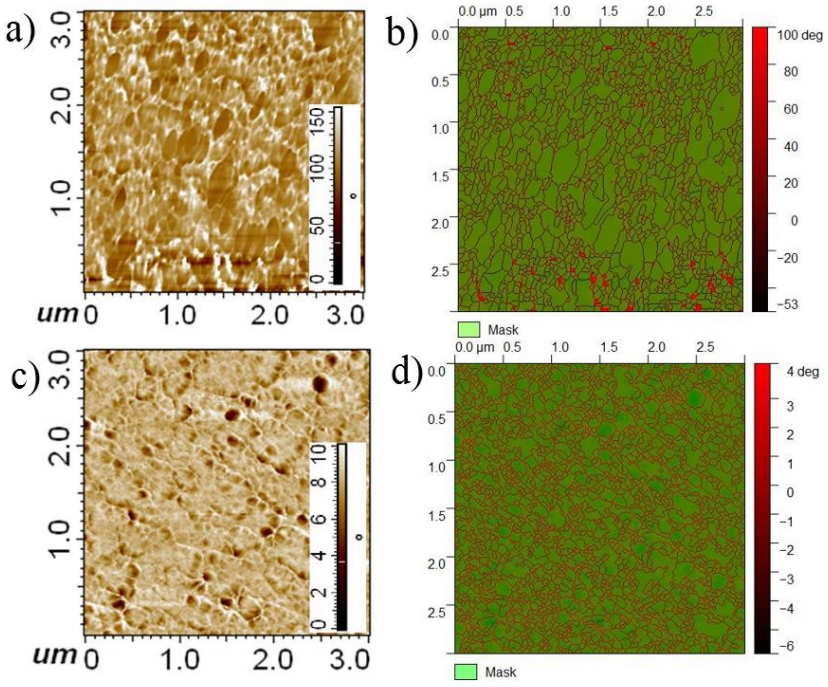

Figure 6.15 Phase contrast micrographs of (a) PIn and (c) Ag-PIn Langmuir film deposited at 30 and 40 mN/m respectively with their corresponding (b) and (d) grain segment.

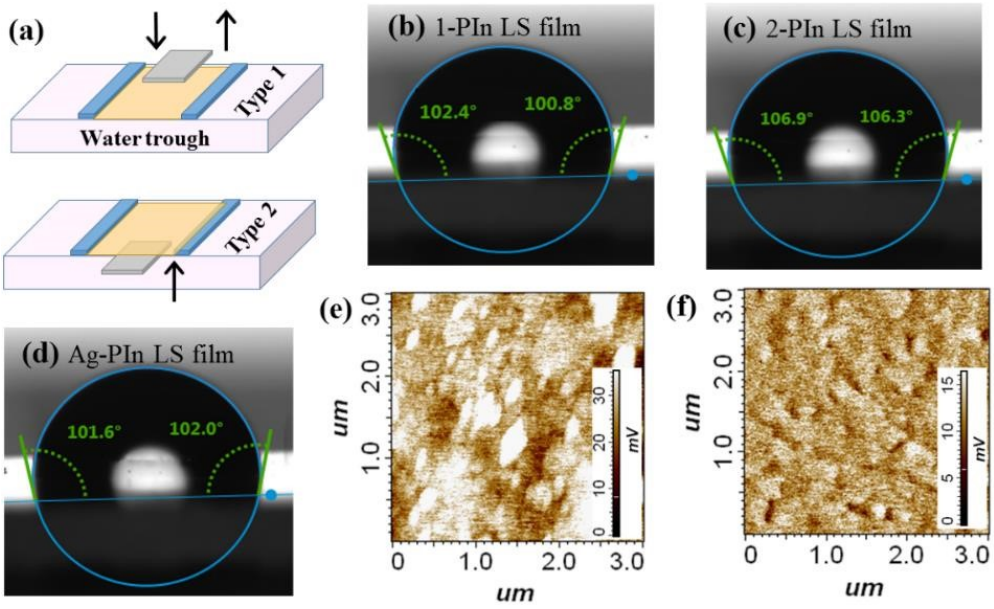

Figure 6.16 (a) Film lifting method of type 1 and 2 for contact angle measurements of LS film of (b) 1-PIn, (c) 2-PIn and (d) Ag-PIn LS films, (e) and (f) Kelvin probe force micrographs of (b) and (d) LS films respectively.

providing it polarity [69]. According to this, Figure 6.16 (b) and (c) clearly support that type 1 are less hydrophobic from type 2 films. This is because when the substrate is stamped from above the water surface, hydrophobic part adheres to it, exposing the hydrophilic part in the air. Whereas in type 2, the substrate already kept beneath the water surface is lifted slowly upwards, adheres hydrophilic part to it. These measurements validate that PIn is suspended at air-water interface with hydrophilic nitrogen part towards the water side. Similar results were seen for Ag-PIn that concludes the wrapping of AgNP by PIn molecules. KPFM images of same surfaces were obtained for both PIn and Ag-PIn LS films lifted from above the water surface. The electrostatic interaction between the Langmuir film surface and AFM tip was monitored in the same region as surface topography, and phase images were scanned. The average for PIn and Ag-PIn Langmuir films are found to be 2.56 mV and 1.373 mV respectively. The decrease in

average contact potential difference, i.e., the increase in work function for Ag-PIn film, measured over an area of 9 μm^2, concludes the homogeneous distribution of AgNP over the polymer sheet [167].

6.2.7 Spectroscopic analysis of Langmuir films

Figure 6.17 represents the absorption spectra of PIn and Ag-PIn LS films. All the transitions for PIn and Ag-PIn LS films such as n-π*, π-π* and polaronic transitions display a red shift as compared to their solution counterparts which are listed in Table 6.3. For the solution state, intra and inter chain interactions are comparatively low than in the solid state [29,55,67,76]. Moreover, Langmuir technique offers a high level of ordering at the interface. Thus this red shift is attributed to the formation of organized structures with extended conjugation length in the LS films.

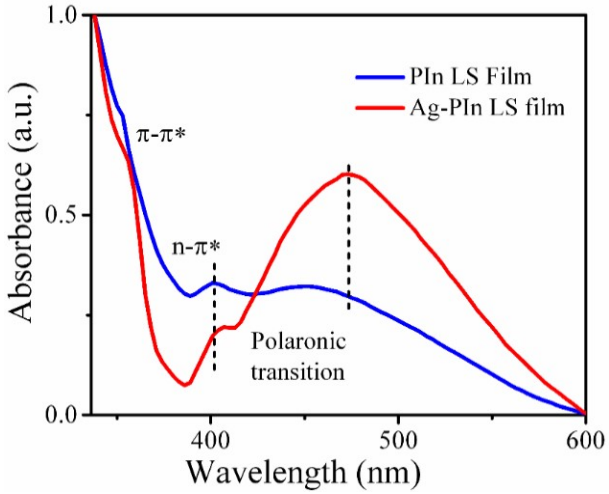

Figure 6.17 UV-vis spectra of LS films (a) PIn and (b) Ag-PIn.

Table 6.3 Characteristic absorptions of PIn and Ag-PIn in their solution and film form.

S.No.	Characteristic absorptions	PIn		Ag-PIn	
		Solution	LS Film	Solution	LS film
1	π-π*	348	353	350	356
2	n-π*	394	401	398	406
3	Polaronic transition	426	450	440	472

In order to investigate the effect of silver NP on polymer film, we have carried out surface enhanced Raman Scattering (SERS) of PIn and Ag-PIn LS films as shown in Figure 6.18.

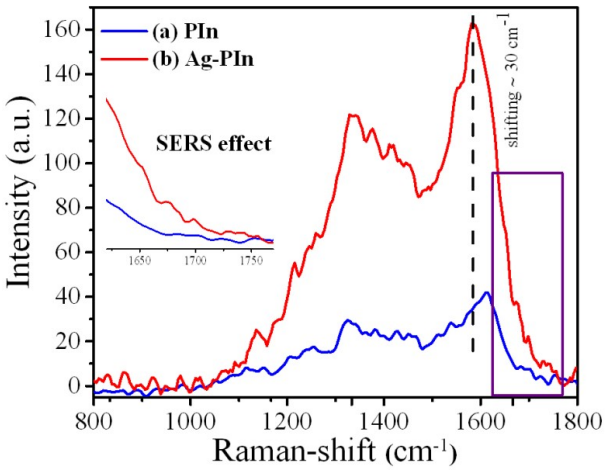

Figure 6.18 Raman spectra of (a) PIn and (b) Ag-PIn LS films (inset: SERs effect)

Raman spectra of PIn LS film (Figure 6.18 (a)) displays characteristic peaks of PIn at 1325 and 1612 cm^{-1} corresponding to C-C stretching and C=C stretching.25,27,40 After silver incorporation in PIn matrix, we could observe a significant shift of 30 cm^{-1} in C=C symmetrical stretching mode (1612 cm^{-1}) towards lower wavenumber and enhancement in intensity (fourfold) of peaks as well (Figure 6.18 (b)).24,25,28,40 This shift and enhancement observed in the Raman signal can be attributed to the existence of an interaction between silver NPs, and SERS phenomena arise due to NPs.

In reported literature, it is mentioned that there are two kinds of enhancement, namely chemical and electromagnetic near field enhancement for any isolated system. For the near field electromagnetic, enhancement must be around 1000 fold which is quite large in comparison to our study [64,99]. However, chemical enhancement must be less than 100 fold. In our case, we observe only four-fold enhancement which can be attributed to chemical SERS. Therefore, this type of enhancement reveals the formation of plasmon-

coupled unified system due to intermolecular interaction between Ag NPs and PIn matrix. In order to further validate the enhancement type, we have conducted XPS which have been discussed in a later section.

6.2.8 Charge transport properties

In order to investigate the electrical and charge transport property across the film, multiple metal-semiconductor devices have been fabricated in a sandwiched structure such as ITO/Ag-PIn/Al and ITO/PIn/Al as illustrated in of Figure 6.19. The J-V characteristics of all samples have been demonstrated in Figure 6.19 (a). Inset of Figure 6.19 (a) shows a semilog plot of J-V characteristics. However, Figure 6.19 (b). shows the J vs V^2 characteristics of same. The J-V characteristics of both devices demonstrate non-linear rectifying behaviour characteristics, which demonstrate the signature of the Schottky diode [41,64,65,66]. The rectifying characteristics of ITO/Ag-PIn/Al were found to be 600% more as compared to pristine film.

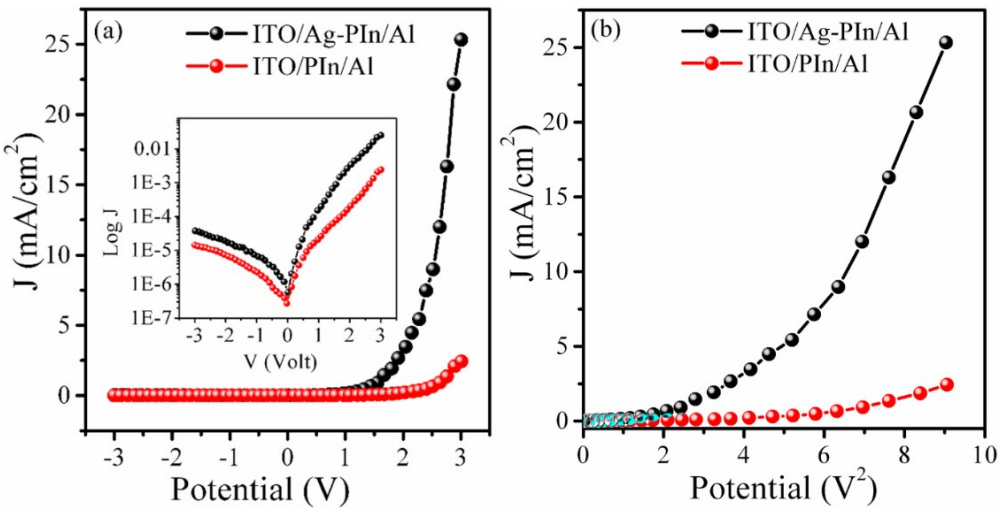

Figure 6.19 Current density-voltage (J-V and J-V^2) characteristics of 5L LS film of pristine PIn and Ag-PIn nanohybrid.

Further, in order to analyse the other electrical parameters such as ideality factor (η),

saturation current (J_0), barrier height (Φ_B), etc. We have employed the thermionic emission theory and Cheung's method by considering the following relations, [18]

$$J = J_0 \exp\left(\frac{qV}{\eta KT}\right) \qquad (6.1)$$

$$J_0 = A^* T^2 \exp\left(-q\varphi_B/KT\right) \qquad (6.2)$$

Where J, J_0, T, V, A*, and η have their usual meaning [76]. However, the intrinsic carrier mobility viz. hole mobility (μ_h) have been determined at higher voltage region from Figure 6.19 (b) and by using the Mott-Gurney equation, [65]

$$J = \frac{9\mu_h \varepsilon_r \varepsilon_0}{8}\left(\frac{V^2}{d^3}\right) \qquad (6.3)$$

Where used symbols have their usual meaning [41]. The parameters of the device have been listed in Table 6.4.

Table 6.4 Out of plane Electrical parameter of devices.

Parameters→ Devices↓	**J_0 (A)**	**Φ_B (eV)**	**H**	**μ_h (cm^2/V.s)**
ITO/Ag-PIn/Al	5.6×10^{-7}	0.83	3.25	7.0×10^{-4}
ITO/PIn/Al	2.67×10^{-7}	0.86	4.65	6.7×10^{-5}

It is noteworthy that ideal diode has η=1 which arises due to following two reasons: (1) carrier drift-diffusion process, (2) Sah-Noyce-Shockley generation-recombination process. However, η of both devices demonstrate greater value as compared to the ideal diode that can be said to arise due to trap aided tunnelling, carrier leakage, and barrier inhomogeneity. Therefore, multilayer deposited LS films with the deviation from ideal behaviour is consistent with our earlier assumptions. However, compositing of PIn with Ag NP induces betterment in the η from 4.65 to 3.23.

Figure 6.19 (a) shows around one order enhancement in forward current for Ag-PIn composite as compared to pristine. However, one order enhancement in intrinsic mobility was observed for the same. In order to understand enhancement in Raman spectra as well as in current density of the Ag-PIn film, XPS measurement of both samples were carried out by targeting N and C. XPS spectra of Ag-PIn and PIn are shown in Figure 6.20. As compared to pristine PIn, N and C peaks for Ag-PIn demonstrated shifting of the peak at a higher binding energy (BE). This shifting of peak discloses the partial charge transfer from polymer backbone to the metal nanoparticle due to the formation of polymer-metal nanoparticle coupled unified system, via chemi-adsorption. This results in an increment in BE of N and C in nanohybrid (Figure 6.20) with a simultaneous decrement in BE (~0.32 eV) of silver (Figure 6.21). Overall, variation in BE validates the partial charge transfer which induces enhancement in intrinsic mobility and forwards current up to one order in composite LS film. To get a better understanding of the effect of interaction between silver and polymer on N1s and C1s spectra of Ag-PIn LS film, their fitted components have been shown in Figure 6.22 [79,99,167]. For N1s spectrum, four main peaks at 399.8, 401.2, 402.6 and 404.5 eV are located (Figure 6.22 (a)) which can be assigned to neutral nitrogen atoms (-NH-), pyrolitic nitrogen peak (N-C, N=C) for lowest BE peak, –NH+ (polaron) and =NH+ (bipolaron) states of the polymer for second and third and fourth peak to the silver interaction with the nitrogen atoms as per previous reports on PIn [99]. Figure 6.19 (b) shows the C1s spectra revealing three different components located at 284.6, 287.5, and 288.5 eV. We assign the lowest binding energy component to C-C, C-H and C-N from Ag-PIn. The second peak at 287.5 eV is designated to carbons of the type, C=N or C-N+, primarily from PIn and the third peak at 288.5 eV corresponds to carbons as C=N+ species due to increased doping in PIn by silver dopant [79,167]. While it is probable that the peaks contain contributions due to interaction (like

hydrogen bonding, van der Waals interaction, etc.) between silver and PIn. So depending on the extent of doping due to silver, there will also be an influence on the binding energies of N and C atoms that is clearly visible in these results. These results are reliable with previous works on PIn in which it was anticipated that the higher BE components correspond to positively charged nitrogen atoms in chemically different environments [21,79,99,167]. Ag in the PIn matrix forms non-covalent interactions with the nitrogen atoms (positively charged) responsible for charge conduction in PIn thus promoting partial charge transfer from PIn towards silver.

In summary, we have designed a schematic (Figure 6.23) that summarizes the impact of slow compression of Langmuir layer forming the large area stable and oriented film on spectral and electrical properties of Ag-PIn nanohybrid. As compared to Pristine PIn, nanohybrid LS displays reduced π-π stacking thus better molecular packing. This betterment is attributed to non-covalent interactions between Ag and PIn chain. Presence of Ag facilitates the uncoiling of PIn molecules thus preventing its aggregation and forming large area assembled film. Interaction between NP and polymer matrix is seen in the form of partial charge transfer from Ag to PIn backbone thus formation of Ag-PIn unified system which causes the enhancement in photophysical and charge transport property of the nanohybrid film. These features contribute to the betterment in device parameters as well as intrinsic mobility of Ag-PIn film.

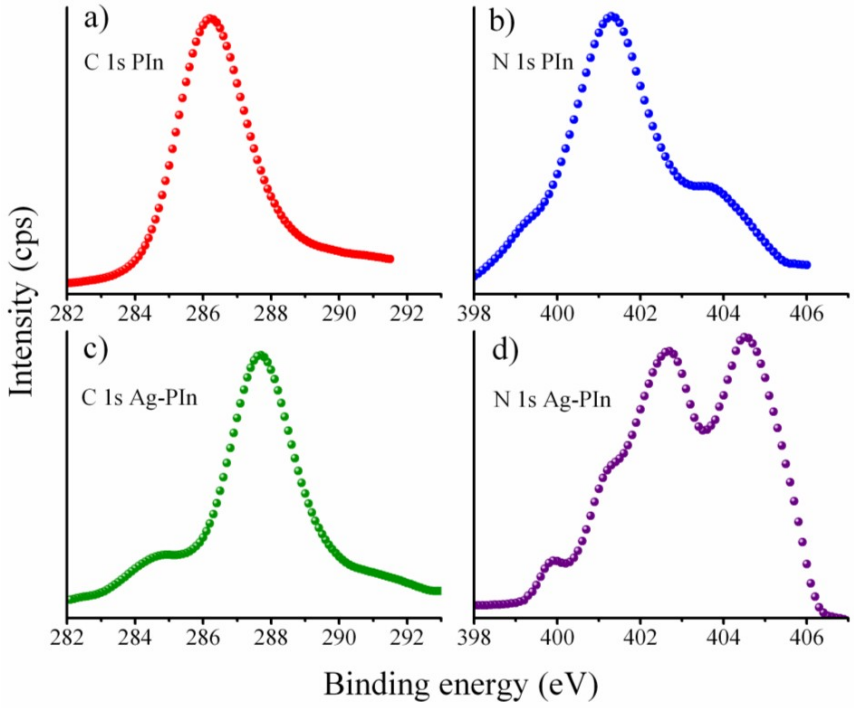

Figure 6.20 XPS spectra of C 1s and N 1s for (a & b) PIn LS film, (c & d) Ag-PIn LS film.

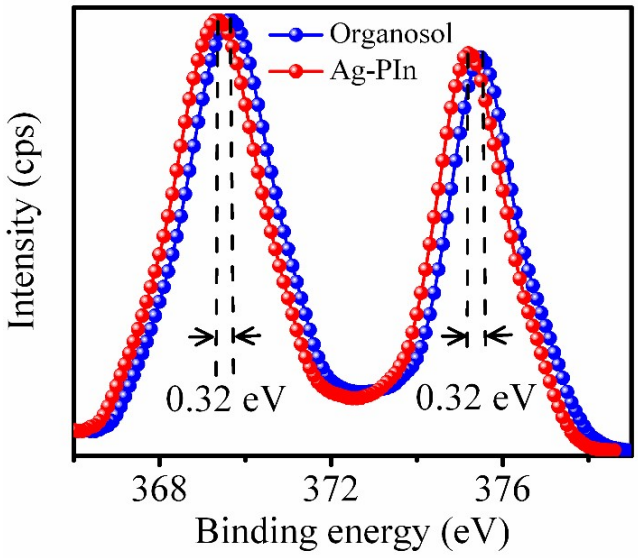

Figure 6.21 XPS spectra for the silver present in organosol and Ag-PIn LS film.

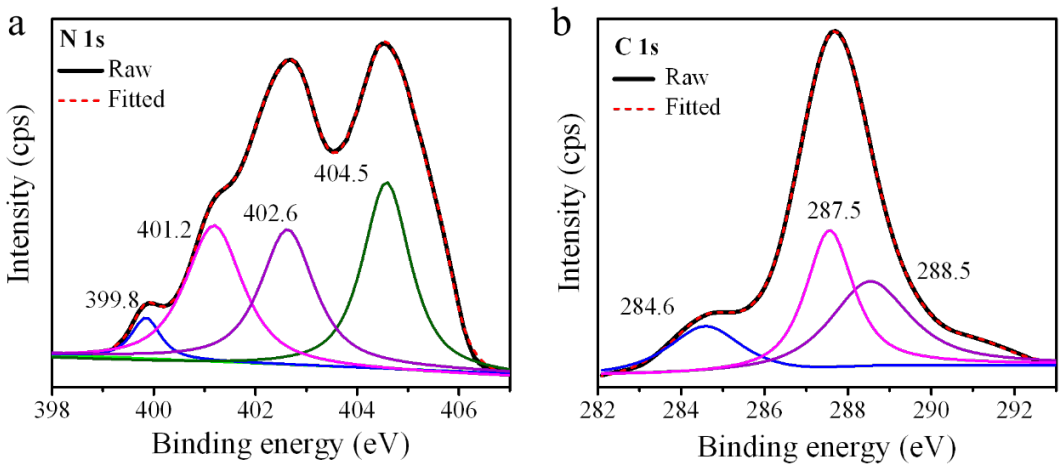

Figure 6.22 XPS spectra of Ag-PIn LS film: (a) N1s and (b) C1s spectrum. Peak positions are mentioned for the fitted components.

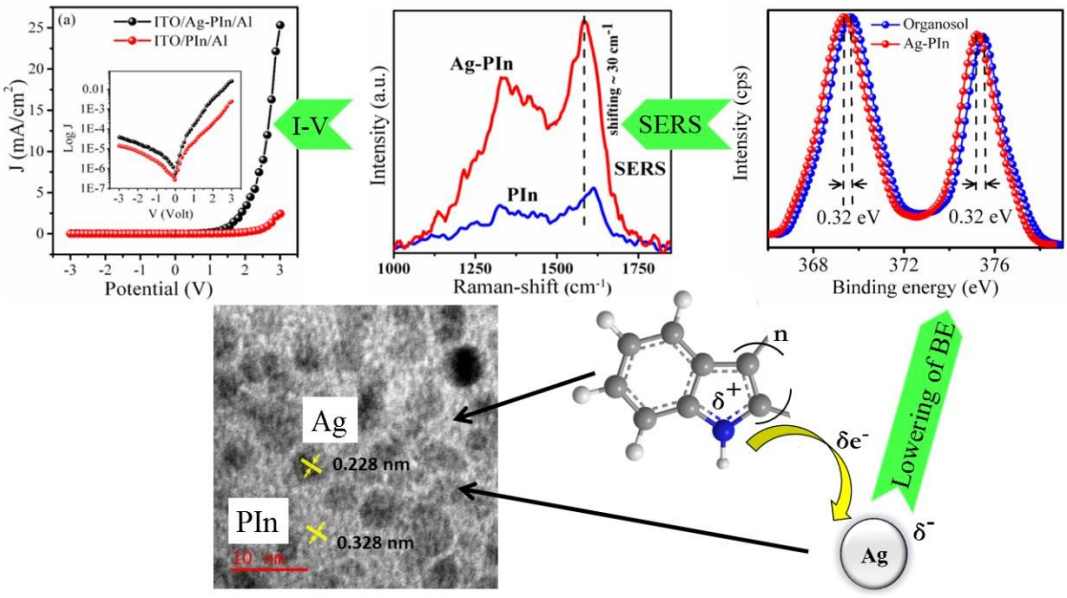

Figure 6.23 Schematic representing the partial charge transfer from PIn to AgNPs resulting in lowering of BE, SERS phenomena and enhancement in charge transport property of Ag-PIn nanohybrid.

6.3 Conclusions

We have achieved a facile, low cost and quick method for attaining solution-processed

AgNPs in organic phase with aid of DDAB serving as PTA and stabilizer both thus eradicating the use of two separate reagents. This DDAB trigerred size-sorted self-assembly of silver NPs approach may head for spontaneously organized electronic applications. Spectral change with a red shift in distinctive silver SPR supported our observation of phase-transfer. Moreover, we also studied the effect of surfactant concentration on PSD and self-assembly of silver NPs in organic phase. Smaller silver core in aqueous phase having higher surface area to volume ratio experienced higher hydrophobic force and switched into organic medium forming larger population of a narrow PSD. The insight provided by reference [160] gives a compelling explanation for the size dependent selectivity of silver NPs stabilization across the water-chloroform interface. XRD and SAED patterns ensured the polycrystallinity of silver and the structural consistency during phase transition of silver NPs. XPS in addition to authorizing the presence of elemental silver complemented FT-IR in establishing the fact related to stabilization of AgNPs through DDAB interaction. It is believed that among the different combinations of DDAB solvents, 25 mM concentration provided us with most appropriate narrow PSD as a function of mentioned parameters. This motivated us to successfully demonstrate the combined role of self-assembling properties of phase transferred AgNP and Langmuir interface technique in obtaining a better-oriented structure of PIn with uniformly dispersed AgNPs in its matrix. Our experiments of compression-relaxation curves and compression-expansion cycles have also validated that the most ordered and stable Langmuir film of Ag-PIn nanohybrid can be obtained at an SP of 40 mN/m. Langmuir films deposited at this SP analysed via microscopic and macroscopic surface analysis techniques displayed the uniform distribution of AgNP in PIn matrix. Furthermore, the interaction between Ag and PIn particularly ascertained from spectroscopic techniques particularly SERS and XPS clearly support the formation

of polymer-metal nanoparticle coupled unified system, via chemi-adsorption thus enhancing the intrinsic mobility of nanohybrid LS film. The present results of this work absolutely confirm the ability of the Langmuir air-water interface methodology and astonishing AgNP self-assembling property to modulate the organization and ordering of various non-alkyl chain containing polymers.